ARTICLE   **Open Access**

Photoreduced nanocomposites of graphene oxide/ N-doped carbon dots toward all-carbon memristive synapses

Ya Lin[1], Zhongqiang Wang[1], Xue Zhang[1], Tao Zeng[1], Liang Bai[2], Zhenhui Kang[2], Changhua Wang[1], Xiaoning Zhao[1], Haiyang Xu [1] and Yichun Liu[1]

Abstract

An all-carbon memristive synapse is highly desirable for hardware implementation in future wearable neuromorphic computing systems. Graphene oxide (GO) can exhibit resistive switching (RS) and may be a feasible candidate to achieve this objective. However, the digital-type RS often occurring in GO-based memristors restricts the biorealistic emulation of synaptic functions. Here, an all-carbon memristive synapse with analog-type RS behavior was demonstrated through photoreduction of GO and N-doped carbon quantum dot (NCQD) nanocomposites. Ultraviolet light irradiation induced the local reduction of GO near the NCQDs, therefore forming multiple weak conductive filaments and demonstrating analog RS with a continuous conductance change. This analog RS enabled the close emulation of several essential synaptic plasticity behaviors; more importantly, the high linearity of the conductance change also facilitated the implementation of pattern recognition with high accuracy. Furthermore, the all-carbon memristive synapse can be transferred onto diverse substrates, showing good flexibility and 3D conformality. Memristive potentiation/depression was stably performed at 450 K, indicating the resistance of the synapse to high temperature. The photoreduction method provides a new path for the fabrication of all-carbon memristive synapses, which supports the development of wearable neuromorphic electronics.

Introduction

Brain-inspired neuromorphic computing is attracting a great deal of attention owing to its high capability for parallel computation and energy efficiency[1−3]. Memristive devices, possessing functional similarity to biological synapses, are regarded as promising candidates for hardware implementation in neuromorphic computing systems[4−7]. Memristive artificial synapses with inherent learning functions have been widely developed. Various materials have been utilized to demonstrate memristive synapses, such as metal oxides[8−10], organics[11,12], chalcogenides[13], and perovskites[14,15]. Among them, carbon-based memristors, as an important component of carbon-based electronics, can be developed into wearable synaptic devices owing to their good mechanical flexibility and transferability[16−18]. Furthermore, all-carbon memristive synapses are expected to exhibit high thermal and chemical stability[19,20], enhancing their adaptability to different application environments. However, some factors limit the development of all-carbon memristive synapses. In many carbon-based synaptic devices, the memristive mechanism depends on the combination of carbon materials with other materials. For example, the migration of ions (e.g., H^+, O^{2-}, and Li^+) from functional layers (e.g., AlO_x and $LiClO_4$ electrolyte) into graphene or carbon nanotubes is capable of tuning the graphene/carbon

Correspondence: Zhenhui Kang (zhkang@suda.edu.cn) or
Haiyang Xu (hyxu@nenu.edu.cn)
[1]Center for Advanced Optoelectronic Functional Materials Research, and Key Laboratory for UV Light-Emitting Materials and Technology (Northeast Normal University), Ministry of Education, 5268 Renmin Street, Changchun, China
[2]Jiangsu Key Laboratory for Carbon-Based Functional Materials and Devices, Institute of Functional Nano and Soft Materials (FUNSOM), Soochow University, Suzhou, China
These authors contributed equally: Ya Lin, Zhongqiang Wang

nanotube conductance in a three-terminal device structure, therefore exhibiting modification of the synaptic weight[21–25]. However, sometimes noncarbon materials are not suitable for the development of flexible and wearable electronics due to the brittleness of inorganic metal-oxide materials.

Graphene oxide (GO) may be a feasible candidate capable of exhibiting resistive switching (RS) via migration of its intrinsic oxygen functional groups[26–28]. In many cases, GO-based memristors generally exhibit digital-type RS (D-RS) between a low-resistance state (LRS) and a high-resistance state (HRS) for memory storage applications. In particular, Liu et al. made significant progress towards all-carbon D-RS memory by employing GO as the active material[29]. Recently, Raeber et al. also demonstrated all-carbon D-RS memory based on amorphous carbon materials[30]. However, analog-type RS (A-RS) with continuous resistance-state variations, which is urgently needed as an essential foundation for the biorealistic emulation of synaptic adaptive functions, has seldom been reported to our knowledge. Both types of memristors have already been proposed to simulate synapses. Compared to D-RS memristors, A-RS memristors with multilevel resistive states present some performance advantages in neuromorphic computing systems designed for complex applications, such as image recognition[31,32]. For example, Garbin et al. demonstrated that a synapse with multilevel resistive states possessed high recognition accuracy for a database of 10,000 handwritten digits compared with that of a synapse with two resistive states[31]. This is because the modulation of synaptic weights is continuous instead of abrupt during the potentiation and depression process in biological neuromorphic systems. Therefore, memristors with gradually changing conductance could be more like biological synapses, which would help to emulate brain functions better. Regarding the memristive mechanism of GO-based devices, D-RS is typically attributed to the formation and rupture of a dominant conductive filament (CF) comprising concentrated oxygen vacancy (V_O)-like defects, termed reduced GO (RGO) domains. In contrast, multiple weak CFs with a large number of localized defects are necessary to produce continuous resistance modulation (i.e., A-RS), as previously proposed[33,34]. Therefore, the controllable generation of local RGO domains may accomplish continuously tunable A-RS in a GO-based memristor, which would make an all-carbon memristive synapse possible. However, the conventional GO reduction methods, such as thermal reduction[35] and chemical reduction[36], generally modify the RGO domains homogeneously throughout the entire film rather than in local regions, which is undesirable for tuning A-RS performance. Furthermore, these methods are generally not compatible with flexible electronic technologies.
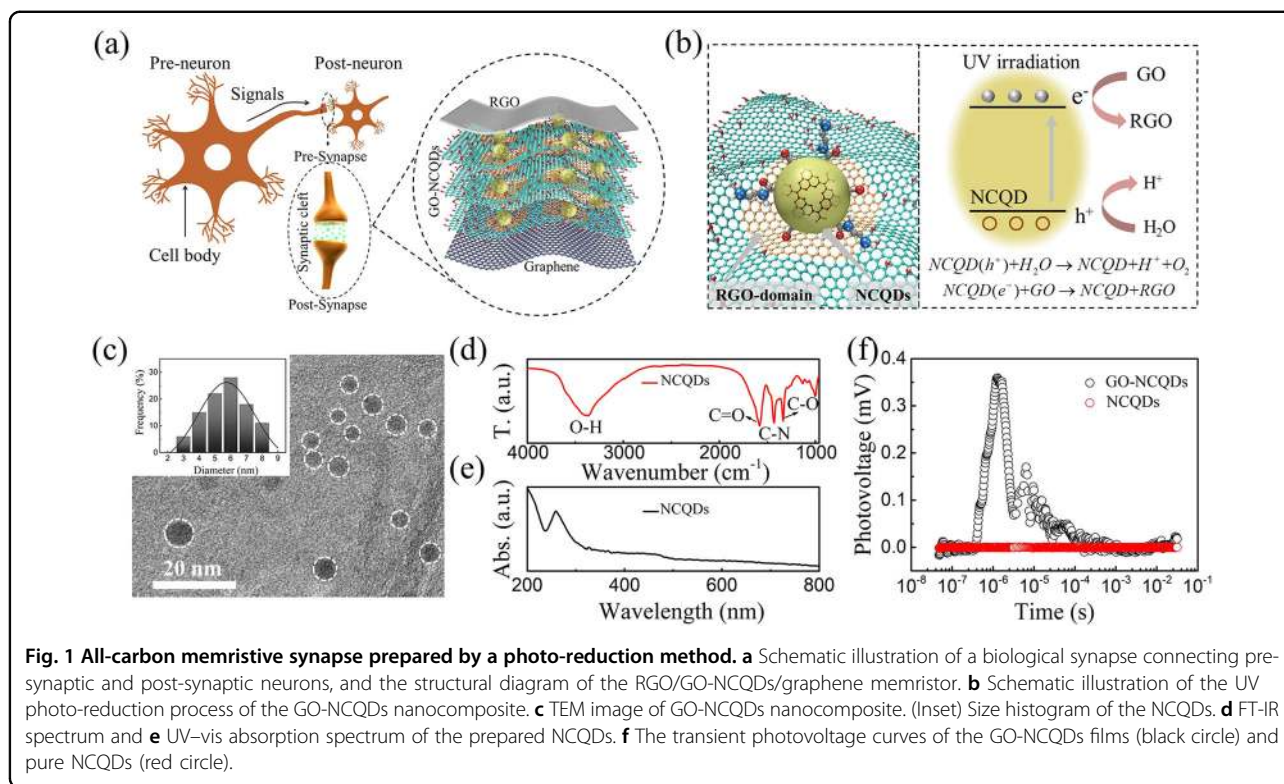
In this work, a simple and mild photoreduction method was conducted by introducing N-doped carbon quantum dots (NCQDs) into GO sheets. Using ultraviolet (UV) light irradiation, the oxygen functional groups near the NCQDs can be dissociated and thereby induce local GO reduction and the demonstration of A-RS behavior. Importantly, an all-carbon memristive synapse was realized using this method that presented an inherent synaptic learning ability and pattern recognition function. Furthermore, the all-carbon memristive synapse possessed good flexibility, transferability, and heat resistance, indicating its excellent potential for application in wearable electronics.

Results and discussion

Figure 1a schematically depicts a biological synapse that connects a presynaptic and postsynaptic neuron. The connection strength of the synapse can respond dynamically under stimulation (i.e., synaptic plasticity), which represents the neurochemical basis for learning and memory functions. The continuous resistance change (i.e., A-RS) of a memristor is analogous to synaptic plasticity. In the present work, our motivation was to develop a GO-based all-carbon memristive synapse with A-RS characteristics, as schematically illustrated in Fig. 1a. An RGO layer and graphene layer on a Cu supporting substrate acted as the top and BEs, and a nanocomposite film of GO and NCQDs (GO-NCQDs) served as the switching layer. Thus, a memristor cell with an RGO/GO-NCQD/graphene sandwich structure was formed, which can be viewed as a biological synapse with a presynapse/synaptic cleft/postsynapse structure. More details about the material synthesis and device fabrication can be found in the "Experimental" section.

The NCQDs used herein were prepared by one-step reflux treatment of C_3N_4 with ethane diamine[37], which can partially retain the ordered microstructure of C_3N_4 (see Fig. S1a in the Supplementary Information). The NCQDs, possessing condensed C–N heterocycles, may thus inherit the high photocatalytic activity of C_3N_4[38,39]. Figure 1c shows a transmission electron microscope (TEM) image of the GO-NCQD nanocomposite, showing that the diameters of the NCQDs were in the range of 2–7 nm. The Fourier transform infrared (FT-IR) spectrum reveals the chemical composition of the NCQDs, as shown in Fig. 1d, primarily exhibiting the absorption bands of O–H bonds at $3368\ cm^{-1}$, C=O bonds at $1585\ cm^{-1}$, and C–O bonds at $1330\ cm^{-1}$. In addition, characteristic C–N vibrations were clearly detected at $1422\ cm^{-1}$. These results suggested that the NCQDs were fragments of C_3N_4 terminated with various functional groups[40]. Figure 1e shows the UV–vis absorption spectrum of the synthesized NCQDs, where the absorption band peak is located in the 240–400 nm region[37]. By using the Tauc plot obtained from the absorption spectrum (see Fig. S1b in the Supplementary Information), the optical

Fig. 1 All-carbon memristive synapse prepared by a photo-reduction method. a Schematic illustration of a biological synapse connecting pre-synaptic and post-synaptic neurons, and the structural diagram of the RGO/GO-NCQDs/graphene memristor. **b** Schematic illustration of the UV photo-reduction process of the GO-NCQDs nanocomposite. **c** TEM image of GO-NCQDs nanocomposite. (Inset) Size histogram of the NCQDs. **d** FT-IR spectrum and **e** UV–vis absorption spectrum of the prepared NCQDs. **f** The transient photovoltage curves of the GO-NCQDs films (black circle) and pure NCQDs (red circle).

band gap (E_g) of the NCQDs was estimated to be 3.3 eV, which is larger than that of bulk C_3N_4 (2.77 eV) owing to the quantum confinement effect[37,40,41]. The above experiment guided us to use UV light to irradiate the film to produce photogenerated carriers; a wavelength range of 320–380 nm was employed herein.

The GO-NCQD films were subjected to a photoreduction process schematically described in Fig. 1b before the deposition of the TEs. UV light (wavelength range: 320–380 nm; power density: 20 mW cm^{-2}) was irradiated directly onto the GO-NCQD film in air (relative humidity: 46%). Under UV irradiation, electron (e$^-$) and hole (h$^+$) pairs were generated in the NCQDs though photo-excitation. Owing to the presence of adsorbed H_2O molecules on the GO surface, the holes reacted with H_2O to produce O_2 and H$^+$. The photogenerated electrons were transferred from the NCQDs to the GO sheets, where they reacted with oxygen functional groups to enable the local reduction of GO. This carrier transfer process was directly supported by transient photovoltage (TPV) measurements. Taking into consideration that pure GO films possess weak TPV responses at long timescales according to previous studies[42–44], it was found in Fig. 1f that the GO-NCQD nanocomposite film showed a sig-nificantly enhanced photovoltaic response, suggesting a prolonged hole lifetime and electron transfer from the NCQDs to the GO. More importantly, because the pho-tocatalytic reduction reaction only occurred near the

NCQDs, local RGO domains were obtained, and their size and density were modulated by the UV irradiation time and NCQD concentration. The distributed RGO domains contributed to the formation of multiple weak CFs in the GO films, providing the foundation for A-RS demon-stration in a GO-based memristor for an all-carbon arti-ficial synapse.

The degree of photoreduction of GO is strongly corre-lated to the quantity of weak CFs inside the GO and to its subsequent A-RS memristive properties. The dependence of the GO photoreduction process on the UV irradiation time (0, 5, 10, and 15 min) was investigated by X-ray photoelectron spectroscopy (XPS) and Raman spectro-scopy. As shown in Fig. 2a, all the C1s XPS spectra of GO without and with UV reduction can be deconvoluted into four peaks corresponding to C–C (284.3 eV), C–O (296.6 eV), C=O (288.1 eV), and O–C=OH (289.8 eV)[45]. To compare the changing trends of these peaks, Fig. 2b plots the evolution of the four carbon bond peaks for varying atomic percentages (at%) as a function of irra-diation time. It can be observed that the C–O and C=O peaks decreased significantly with irradiation time, indi-cating reduction from GO to RGO. Furthermore, Raman spectroscopy verified the gradual increase in the RGO domain size with increasing irradiation time, as shown in Fig. 2c, featuring D- and G-bands located at 1356 and 1591 cm^{-1}, respectively. The ratio of the D- and G-band intensities (I_D/I_G) clearly increased from 0.91 to 1.12 with
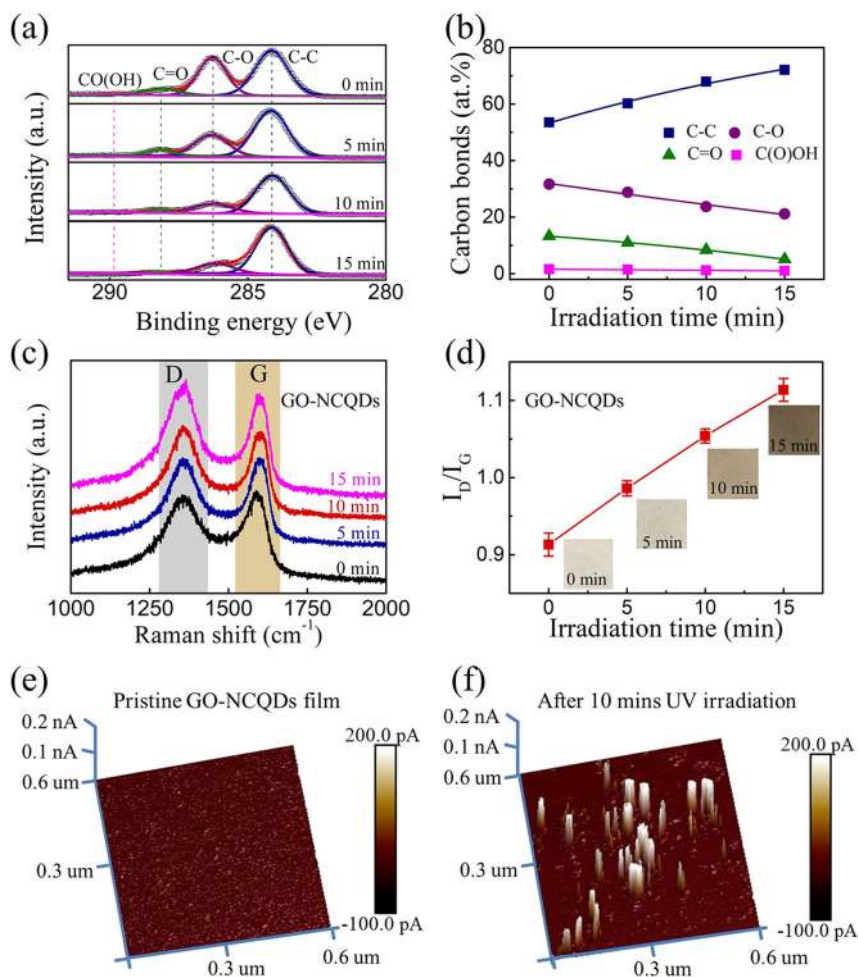
Fig. 2 Characterizations of the photoreduction process of GO-NCQDs nanocomposites. a XPS spectra of C1s core level and **b** atomic percentage of different carbon bonds in GO-NCQDs composites after undergoing various UV irradiation times of 0, 5, 10, and 15 min. **c, d** Raman spectra and peak intensity ratio (I_D/I_G) of GO-NCQDs thin film after UV reduction for 0, 5, 10, and 15 min. The inset shows the pictures of the GO-NCQDs thin film undergoing different irradiation time. **e, f** The current distribution measured by CAFM mapping of the **e** pristine GO-NCQDs film and **f** 10 min UV-irradiated GO-NCQDs film. Both measurements were conducted in a scanning area of $0.6 \times 0.6\ \mu m^2$ with a read bias of 10 mV.

increasing irradiation time, indicating an enlargement of RGO domains[46,47]. The color of the GO-NCQD film changed from light brown to black with increasing irradiation time, also indicating an increase in RGO domains (inset of Fig. 2d). More importantly, the RGO domains were formed locally around the NCQDs, which was confirmed by measuring the distribution of local conductivity in the GO-NCQD film using conductive atomic force microscopy (CAFM). Figure 2e shows the pristine GO film, which exhibits a uniform distribution of low conductivity in the absence of UV irradiation. In contrast, the film after 10 min UV irradiation contained many local bright regions corresponding to relatively high conductivity regions, which indicated the existence of local RGO domains (Fig. 2f). These RGO domains act as linking sites, contributing to the formation of multiple weak

CFs in a memristive device. In addition, one might argue that even if no NCQDs are introduced, GO can also be reduced by UV light. However, this possibility is unlikely because the ratio of I_D/I_G in the Raman spectrum did not change obviously for the pure GO film under long-term UV irradiation (see Fig. S2 in the Supplementary Information). It is worth noting that the photoreduction capability of a film is dependent on the humidity of the environment. The reduction capability of films under different humidity conditions is presented in Fig. S3 in the Supplementary Information. A high-humidity environment facilitated the reduction process with the same irradiation time.

As expected, the all-carbon memristor with the RGO/GO-NCQDs/graphene structure demonstrated A-RS behavior after a certain UV irradiation duration. Figure 3a, b
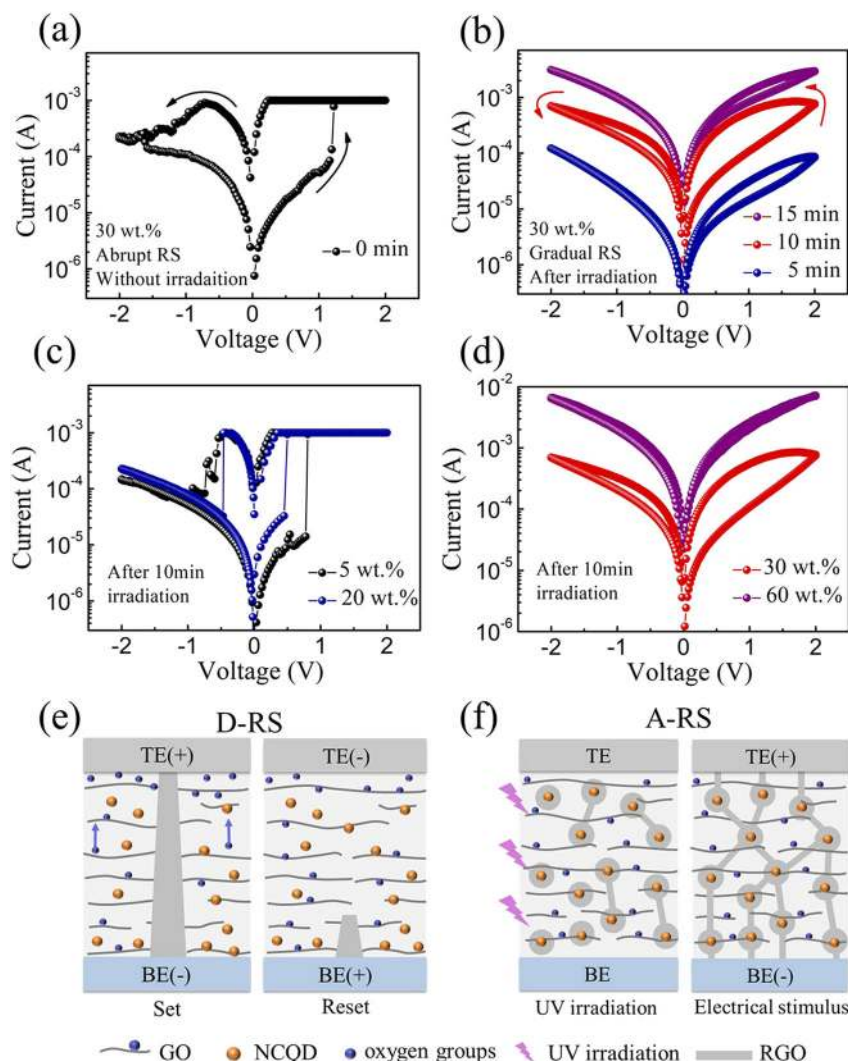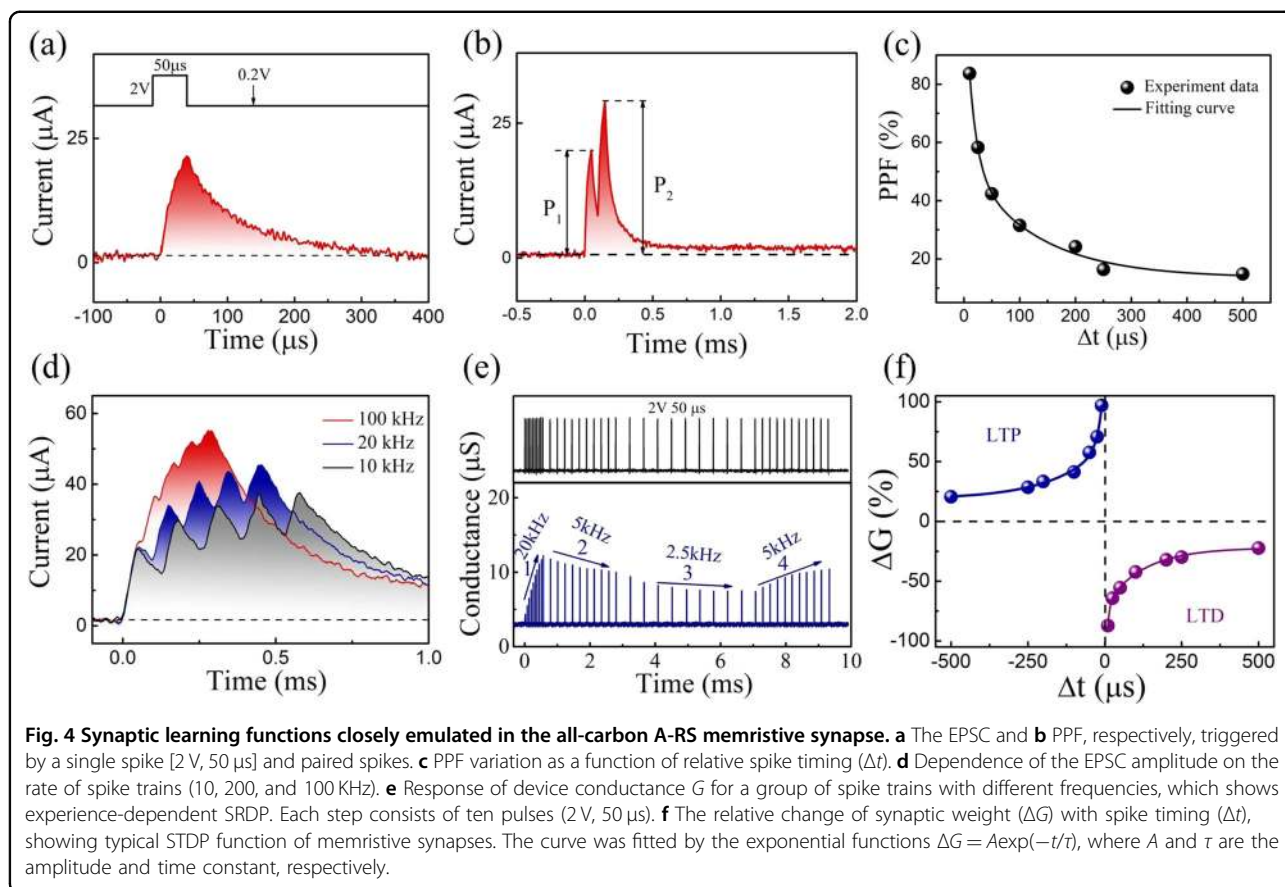
Fig. 3 A-RS memristive behavior realized by optimizing UV irradiation time and NCQDs concentration. a, b *I–V* characteristic of the RGO/GO-NCQDs/graphene memristor without UV irradiation (**a**) and with (**b**) 5, 10, and 15 min UV irradiation. The NCQDs concentration is fixed at 30 wt%. **c, d** *I–V* characteristic of UV-irradiated memristor with different NCQDs concentration of **c** 5 and 20 wt%, and **d** 30 and 60 wt%. The irradiation time is fixed at 10 min. **e, f** Schematic diagrams of the **e** D-RS and **f** A-RS mechanism showing dominant CF and multiple weak CFs, respectively.

shows a comparison of the memristive characteristics of devices with varying UV irradiation durations (0, 5, 10, and 15 min), where an NCQD concentration of 30 wt% was used. For the pristine device (without irradiation), only D-RS behavior was obtained after the formation process (see Fig. S4 in the Supplementary Information), in which an abrupt transition between HRS and LRS occurred reversibly under the positive/negative voltage sweep. In contrast, the devices after UV irradiation presented gradual memristive switching (i.e., A-RS) during the voltage sweep, with stable operation when the device size was scaled down (see Fig. S5 in the Supplementary Information). Furthermore, the operation current of A-RS can be enhanced with increasing UV irradiation time owing to RGO domain enlargement. However, the small increase in current during the positive voltage

sweep for the device after 15 min of irradiation was because of the formation of excessive RGO domains, which could increase the leakage current of the film. The enhancement in conductance tends towards saturation during the voltage sweep, which leads to a small switching window. When the irradiation time was short (below 5 min), a small amount of RGO domains were generated, indicating an insulation state of the film. The energy during the 2 V voltage sweep was just enough for the formation of conductive RGO domains but was not enough to form multiple weak CFs. Thus, the current increase was not obvious in the device under a short irradiation time.

Note that the NCQD concentration in the GO sheets also strongly impacted the RS behavior. Specifically, at low NCQD concentrations (5 and 20 wt%), the device only

Fig. 4 Synaptic learning functions closely emulated in the all-carbon A-RS memristive synapse. a The EPSC and **b** PPF, respectively, triggered by a single spike [2 V, 50 μs] and paired spikes. **c** PPF variation as a function of relative spike timing (Δt). **d** Dependence of the EPSC amplitude on the rate of spike trains (10, 200, and 100 KHz). **e** Response of device conductance G for a group of spike trains with different frequencies, which shows experience-dependent SRDP. Each step consists of ten pulses (2 V, 50 μs). **f** The relative change of synaptic weight (ΔG) with spike timing (Δt), showing typical STDP function of memristive synapses. The curve was fitted by the exponential functions $\Delta G = A\exp(-t/\tau)$, where A and τ are the amplitude and time constant, respectively.

exhibited D-RS behavior, even after 10 min UV irradiation (see Fig. 3c). With an increase to a moderate concentrations of 30 wt%, A-RS behavior started to appear. However, a higher NCQD concentration of 60 wt% or above could lead to the formation of excessive RGO domains, thereby eliminating the A-RS window. In addition, the thickness of the GO-NCQD film also influences the A-RS behavior, and a film of approximately 100 nm is optimal to obtain an appropriate switching window (see Fig. S6 in the Supplementary Information). Thus, to optimize the A-RS window, a UV irradiation time of 10 min and an NCQD concentration of 30 wt% were selected as the optimal conditions in subsequent experiments. These devices possessed reliable and reproducible synaptic properties except for some acceptable fluctuations (see Fig. S7 in the Supplementary Information). The mechanism of transition from D-RS to A-RS can be understood in the following way. As schematically shown in Fig. 3e, D-RS can be generally attributed to the formation and rupture of a dominant CF inside the GO. The initial electroforming process plays a role in generating this dominant CF by inducing the migration of oxygen functional groups under an electric field[48]. In comparison, local RGO domains were generated via UV irradiation, and the CFs preferentially grew around the RGO domains

due to the local electric field enhancement effect[49]. Connections among these domains can be regarded as multiple weak CFs for A-RS, as illustrated in Fig. 3f. Thus, the device conductance can be continuously adjusted by controlling the number of these multiple weak CFs, which is similar to a model involving modulation of the number of CFs[34].

The A-RS characteristics of our all-carbon-based memristor enabled a close emulation of synaptic learning functions. The device conductance G was treated as the synaptic weight in the present work. Figure 4a shows the current response of the A-RS memristive device under a single presynaptic spike [2 V, 50 μs]. A single stimulation induced an initial abrupt increase and a subsequent decay in current, which has a good resemblance to the excitatory postsynaptic current (EPSC) in a biological synapse[5,50]. This phenomenon can be attributed to the dynamic process of oxygen groups (drift and diffusion) in the A-RS memristor. The dynamic process during the evolution of CFs has been investigated in previous studies. For example, Kim et al. directly observed nanoscale conductive graphitic channels in GO films by using low-voltage spherical-aberration-corrected transmission electron microscopy, and they verified through a Raman intensity ratio map that these RGO CFs are induced by
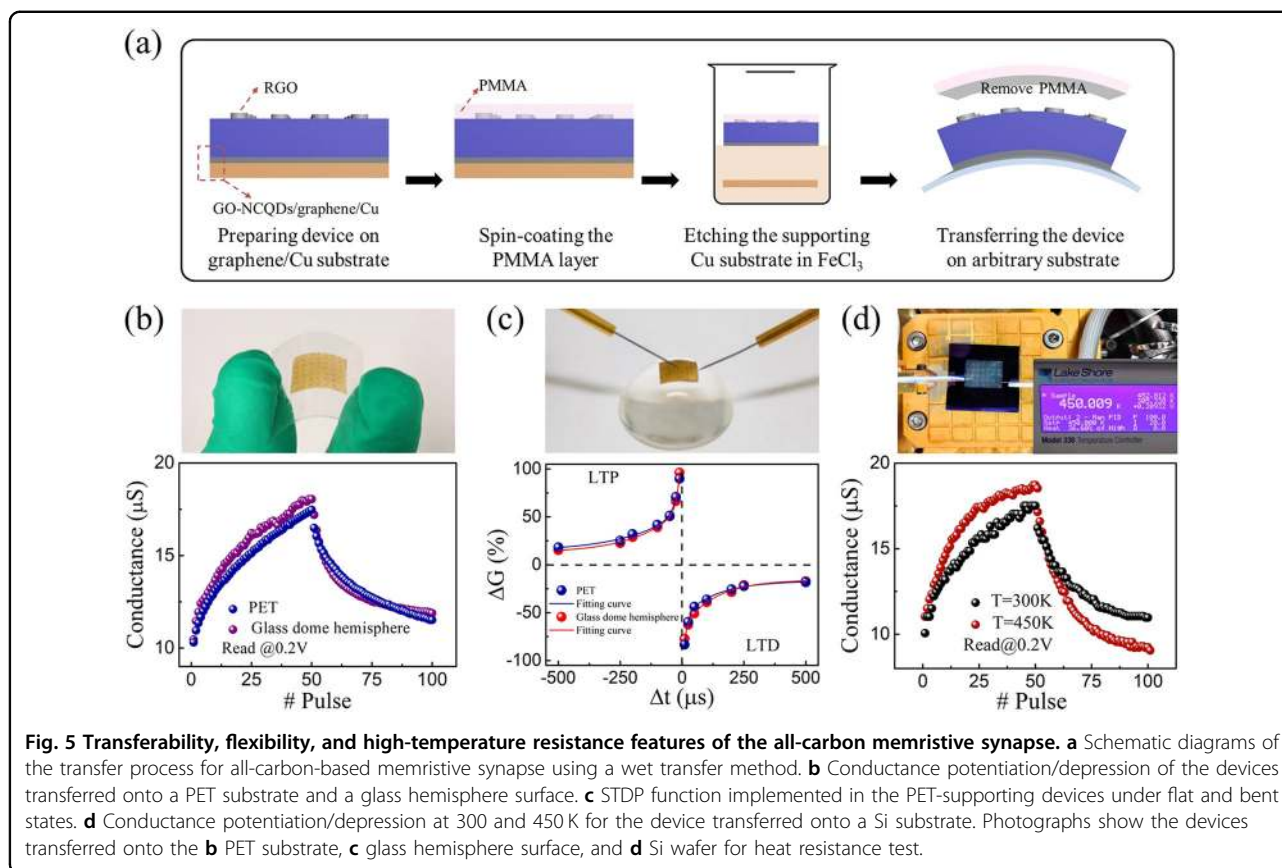
the detachment of oxygen groups[28]. In our work, the partial spontaneous rupture of multiple weak CFs is ascribed to the appearance of oxygen-group diffusion, which was generally absent in the case of the dominant CF for the D-RS memristor (see Fig. S8a in the Supplementary Information). Importantly, if a second presynaptic spike was introduced before the EPSC induced by the first spike decayed to zero, these two nonoverlapping spikes can cause a correlation, effectively suppressing the spontaneous diffusion of oxygen groups, thereby enhancing the conductance change. This kind of decay process is therefore considered an indicator of a second-order memristor[34,51,52] that can demonstrate the essential synaptic functions of short-term paired-pulse facilitation (PPF) and long-term spike-timing-dependent plasticity (STDP). As illustrated in Fig. 4b, the PPF function was emulated using a pair of spikes (P1 and P2), in which the EPSC induced by the second spike P2 was clearly higher than that of the first spike P1. A shorter interval time between these two spikes led to greater synaptic facilitation (as shown in Fig. 4c), which is consistent with the behavior of a biological synapse[53–55].

Spike-rate-dependent plasticity (SRDP) is another critical synaptic function and was emulated using a spike train instead of a spike pair in our A-RS memristor. As shown in Fig. 4d, a much higher EPSC amplitude can be obtained under stimulation with a higher spike rate, which is similar to the case of SRDP in a biological synapse. Furthermore, it is interesting to note that synaptic learning is experience-dependent; namely, identical spike trains can induce either potentiation or depression of synaptic weight depending upon the history of synapse stimulation. Herein, experience-dependent synaptic plasticity was also mimicked using a four-step procedure, as shown in Fig. 4e. In this procedure, 4 groups of 10 spikes with frequencies of 20, 5, 2.5, and 5 kHz were applied to the memristor. In step 1, the spike train with a relatively high frequency of 20 kHz enhanced the conductance to a high value of $G_1 = 12.5\,\mu S$, which was regarded as the first learning experience for subsequent measurements. In step 2, the spike train with 5 kHz frequency caused a decrease in device conductance to $10.2\,\mu S$ (i.e., depression). In step 3, the spike train with 2.5 kHz frequency induced a conductance of $G_2 = 7.5\,\mu S$, acting as another learning experience for the next step (4). In step 4, a spike train with 5 kHz frequency was again applied for stimulation, inducing an enhancement in conductance to $11\,\mu S$ (i.e., potentiation). This potentiation behavior in step 4 was clearly different from the depression behavior observed in step 2, although the same spike train was used. This opposite behavior of depression and potentiation for steps 2 and 4 can be related to the different learning experiences represented by G_1 and G_2 in steps 1 and 3. This experience-dependent adaptation

function offers the opportunity to reproduce the Bienenstock–Cooper–Munro learning rule, which is an important type of SRDP and further describes experience-dependent synaptic modification[56–58]. It is worth noting that the duration time of applied stimuli shows a great influence on memristive behavior as well as frequency. A long stimulus time was the most effective for the enhancement of conductance, which is presented in Fig. S9 in the Supplementary Information.

EPSC and PPF are generally kinds of short-term plasticity, whereas a relatively large PPF can also induce a conversion from short-term plasticity to long-term plasticity, as shown in Fig. 4b. The long-term retention data of PPF are presented in Fig. S10 in the Supplementary Information. Based on this result, long-term STDP, representing the Hebbian learning rule, was demonstrated in the all-carbon memristive synapse, as illustrated in Fig. 4f. In this demonstration, a pair of pulses [$V+/V- = 2\,V/-2\,V$, 50 μs] was applied on the top and BEs as pre- and postsynaptic spikes (see Fig. S8b in the Supplementary Information)[5]. The conductance change ΔG was collected using a reading pulse [$+0.2\,V$, 50 μs] with a delay time of 60 s after the stimulations to ensure a readout of the long-term effect. The change in synaptic weight (ΔG) strongly depended on the time delay and the time interval between the pre- and postsynaptic spikes. Long-term potentiation occurred when the presynaptic spike was earlier than the postsynaptic spike (i.e., $\Delta t < 0$), while long-term depression occurred at $\Delta t > 0$. Moreover, ΔG changed exponentially with the interval time Δt following an exponential equation.
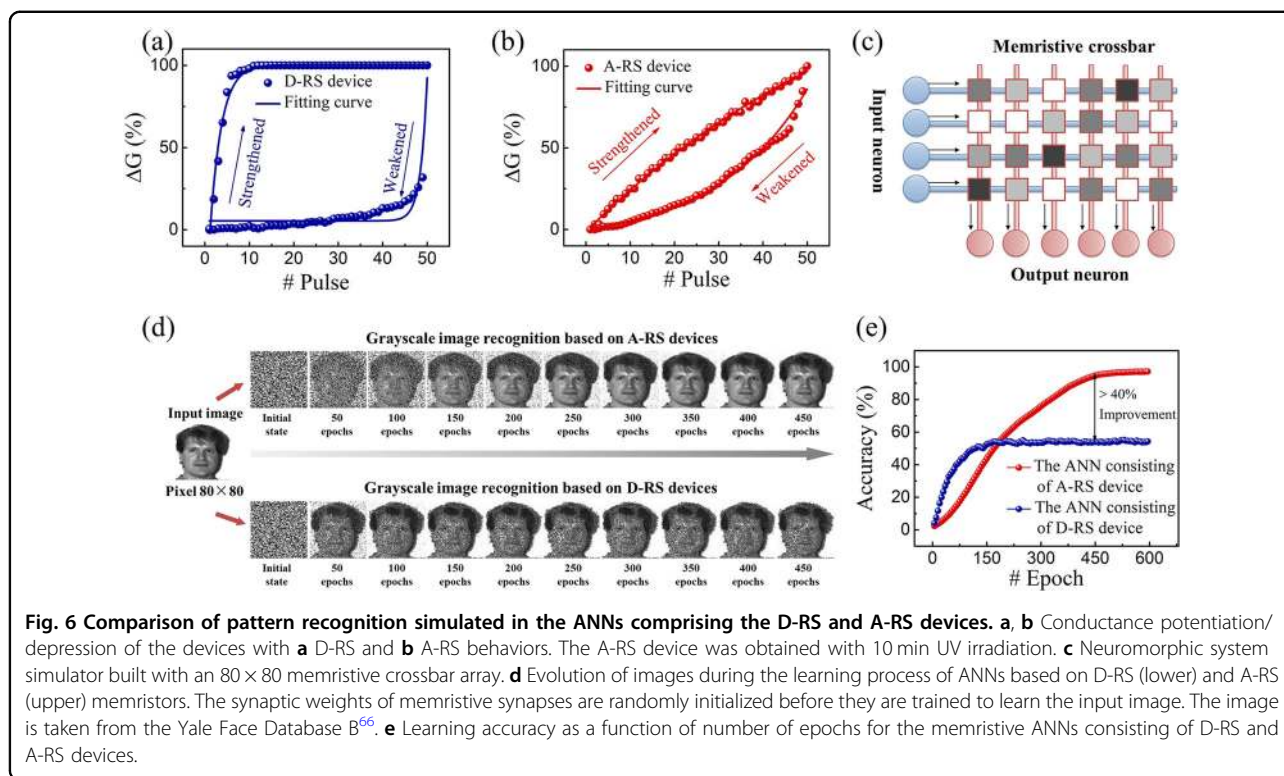
The all-carbon memristive synapse herein further demonstrated features of flexibility, transferability, and heat resistance due to some excellent properties of graphene-based materials. For this demonstration, a free-standing memristor comprising RGO/GO-NCQDs/graphene was prepared using a wet transfer method[59,60]. As illustrated in Fig. 5a, this method included four main steps, and the details are presented in the "Experimental" section. As shown in Fig. 5b–d, the device can be adhered onto different surfaces without visible damage, such as poly(ethylene terephthalate) (PET), a glass dome hemisphere and a silicon wafer, due to the good mechanical properties of the all-carbon materials and the high van der Waals forces at the interface[61,62]. A repeated bending test was also carried out over 5×10^3 times for the memristive device (see Fig. S11 in the Supplementary Information). There was no significant change in the potentiation/depression behavior with bending cycles, suggesting excellent flexibility against mechanical strain. Such stable pulse-induced potentiation/depression, as well as the typical STDP function, can also be achieved in PET-supported devices in the bent state (the bending radius and strain level were 5.2 mm and 1.9%, respectively). No

Fig. 5 Transferability, flexibility, and high-temperature resistance features of the all-carbon memristive synapse. a Schematic diagrams of the transfer process for all-carbon-based memristive synapse using a wet transfer method. **b** Conductance potentiation/depression of the devices transferred onto a PET substrate and a glass hemisphere surface. **c** STDP function implemented in the PET-supporting devices under flat and bent states. **d** Conductance potentiation/depression at 300 and 450 K for the device transferred onto a Si substrate. Photographs show the devices transferred onto the **b** PET substrate, **c** glass hemisphere surface, and **d** Si wafer for heat resistance test.

obvious difference in device performance was observed between the flat and bent devices, demonstrating excellent flexibility and 3-D conformality of the all-carbon memristor for applications in wearable electronics. Furthermore, the all-carbon memristive synapse possesses resistance to high temperature due to the good thermal conductivity and thermal stability of graphene-based layered materials[19,63,64]. The device was transferred onto a Si substrate and then heated to a high temperature of 450 K. As shown in Fig. 5d, the synaptic weight of our memristive synapse maintained continuous potentiation/depression under positive/negative pulses at 450 K. Based on a 2D heterostructure of graphene/$MoS_{2-x}O_x$/graphene, Miao's group demonstrated a robust D-RS memristor with ultrahigh thermal stability and partly attributed the heat resistance to the graphene electrodes and the atomically sharp interface[65]. These results suggest that carbon-based memristors, as neuromorphic computing units, have the potential for use in future high-temperature harsh-environment electronics.

It is worth noting that our all-carbon memristor with A-RS characteristics exhibited a much higher linearity in synaptic weight changes (i.e., ΔG, conductance changes) than did that with D-RS characteristics, as illustrated in Fig. 6a, b, which shows the strengthened/weakened ΔG

induced by positive/negative voltage pulses (2 V, 50 μs/ −2 V, 50 μs) for the pristine D-RS device and the UV-irradiated A-RS device. This relatively high linearity is considered a key advantage for pattern recognition applications. To investigate the pattern recognition ability of our all-carbon memristor, an artificial neuromorphic network (ANN) simulator was developed using an 80×80 memristive crossbar array, as shown in Fig. 6c. Herein, each memristor cell served as a synapse to connect pre- and postneurons, where the synaptic weight of each memristor was represented by the gray level of each pixel. The learning processes of the D-RS and A-RS devices followed the changes in ΔG shown in Fig. 6b, c. A single grayscale image was chosen as an input image for pattern learning[66]. Figure 6d shows a comparison of the image evolution with the learning epochs for these two devices. It can be seen that the ANN comprising the A-RS device possessed higher learning accuracy. For quantitative analysis, the learning accuracy can be represented as the difference between the input and obtained images (see "Experimental" section). As shown in Fig. 6e, the learning accuracy of the ANN comprising A-RS devices was 96.7%, which was 40% higher than that of the ANN comprising D-RS devices. The higher linearity of the conductance change of the A-RS device may be responsible for the

Fig. 6 Comparison of pattern recognition simulated in the ANNs comprising the D-RS and A-RS devices. a, b Conductance potentiation/depression of the devices with **a** D-RS and **b** A-RS behaviors. The A-RS device was obtained with 10 min UV irradiation. **c** Neuromorphic system simulator built with an 80 × 80 memristive crossbar array. **d** Evolution of images during the learning process of ANNs based on D-RS (lower) and A-RS (upper) memristors. The synaptic weights of memristive synapses are randomly initialized before they are trained to learn the input image. The image is taken from the Yale Face Database B[66]. **e** Learning accuracy as a function of number of epochs for the memristive ANNs consisting of D-RS and A-RS devices.

improved learning accuracy[30,67,68]. This result indicates that the all-carbon A-RS memristor has the capability for pattern recognition with high accuracy.

Conclusion

We experimentally demonstrated an all-carbon memristive synapse with A-RS behavior for the first time by introducing NCQDs into GO films and subsequently treating the films with UV irradiation. This photocatalytic method induced a local reduction of GO around the NCQDs, which allowed the memristive behavior to be changed from D-RS to A-RS. The A-RS characteristics were optimized via the UV irradiation time and NCQD concentration, thus enabling the emulation of several synaptic functions, such as EPSC, PPF, and STDP. In particular, interesting experience-dependent SRDP behavior was demonstrated. Owing to the high linearity of the synaptic weight changes in the A-RS device, the memristive ANNs possessed a high accuracy of up to 96.7% for pattern recognition. This all-carbon-based memristive device could be transferred onto a flexible substrate and curved surface, exhibiting flexibility, 3D conformality and transferability. Furthermore, the device can still demonstrate memristive behavior at 450 K, exhibiting good resistance to high temperature. This work offers an approach for the development of an all-carbon memristive synapse, which is beneficial for exploring wearable neuromorphic computing systems in the future.

Materials and methods
Synthesis of GO-NCQD composite

(1) The NCQDs were synthesized via a one-step wet chemical method using C_3N_4 powder[37], whereby 0.02 g C_3N_4 power was added to 10 mL of ethane diamine to form a suspension, which was refluxed for 12 h at 80 °C. The pH of the mixture solution was adjusted to 7 with HCl and then treated by dialysis using a semipermeable membrane to obtain pure NCQDs. (2) GO sheets were synthesized by the modified Hummers method. Graphite powder (2 g) and H_2SO_4 (98%, 50 mL) were mixed. The mixture was then cooled to 0 °C in an ice bath, followed by the slow addition of $KMnO_4$ (7 g) and subsequent dilution with 400 mL deionized (DI) water. Next, hydrogen peroxide (H_2O_2, 30%) was slowly added to the mixture accompanied by stirring until gas evolution stopped. The solution was then filtered and washed, first with HCl (30%, 1 mL) and then with DI water, until the filtrate was neutral. Finally, the slurry was dried to yield GO powder. (3) NCQDs and GO (10 mg) were added to 100 mL DI water, and the mixture was stirred for 1 h to obtain a homogeneous suspension. To investigate the impact of the NCQD concentration on the memristive behavior, the weight of the NCQDs in the GO-NCQD nanocomposite was varied at 5, 20, 30, and 60 wt%.

Preparation of all-carbon-based memristive synapses

Graphene on a copper foil substrate was chosen as the bottom electrode (BE). Next, the GO-NCQD composite

was spin-coated onto the graphene substrate layer, and the film was baked at 60 °C for 1 h to remove any remaining solvent. The thickness of the GO-NCQD film was measured to be approximately 100 nm by a step profiler (KLA-Tencor Corporation D-120). During the photoreduction process, the film was irradiated by UV light (Hayashi LA-410UV, 5 mW cm^{-2}) for various durations (0, 5, 10, and 15 min) directly in air. Finally, the RGO top electrodes (TEs) were sprayed as a top layer and patterned using a shadow mask into multiple circular pads 200 μm in diameter.

Preparation of a transferable memristive synapse

First, the device was prepared on a Cu substrate. Second, the as-prepared device was spin-coated with a polymethyl methacrylate (PMMA) layer to protect it from damage during the transfer process. Third, the Cu layer was dissolved by immersing the device into a ferric chloride (FeCl$_3$) solution for 2 h, where upon the RGO/GO-NCQDs/graphene device was delaminated from the Cu substrate. Subsequently, the device was transferred onto various substrates; the PMMA layer was removed by putting the device into acetone solution in advance.

Electrical measurements

$I-V$ measurements were carried out using a Keithley 2636A source meter, while pulse measurements were obtained using an arbitrary function generator (3390, Keithley) and a digital oscilloscope (Keysight DSOS404A). The distribution of local conductivity was measured by CAFM (Dimension Icon, Bruker). Temperature-dependent testing was carried out in a probe station with a temperature controller (Lake Shore TTPX).

Calculation of pattern recognition accuracy

Structural similarity (SSIM) was employed to calculate the similarity between the learned image (x) and the input image (y). Herein, a high SSIM value can directly represent a high learning accuracy. The SSIM can be expressed as

$$\mathrm{SSIM}(x,y) = f(l(x,y), c(x,y), s(x,y)), \quad (1)$$

where $l(x, y)$, $c(x, y)$, and $s(x, y)$ are the brightness, contrast, and structure of the image, respectively. A detailed explanation of this metric can be found in the literature[69].

Conflict of interest
The authors declare that they have no conflict of interest.

References
1. Wang, Y. et al. Photonic synapses based on inorganic perovskite quantum dots for neuromorphic computing. *Adv. Mater.* **30**, 1802883 (2018).
2. Sun, L. et al. Synaptic computation enabled by joule heating of single-layered semiconductors for sound localization. *Nano Lett.* **18**, 3229–3234 (2018).
3. Zidan, M. A., Strachan, J. P. & Lu, W. D. The future of electronics based on memristive systems. *Nat. Electron.* **1**, 22 (2018).
4. Wang, Z. et al. Memristors with diffusive dynamics as synaptic emulators for neuromorphic computing. *Nat. Mater.* **16**, 101 (2017).
5. Wang, Z. Q. et al. Synaptic learning and memory functions achieved using oxygen ion migration/diffusion in an amorphous InGaZnO memristor. *Adv. Funct. Mater.* **22**, 2759–2765 (2012).
6. Liu, G. et al. Organic biomimicking memristor for information storage and processing applications. *Adv. Electron. Mater.* **2**, 1500298 (2016).
7. Park, Y. & Lee, J.-S. Artificial synapseFs with short-and long-term memory for spiking neural networks based on renewable materials. *ACS Nano* **11**, 8962–8969 (2017).
8. Yang, R. et al. On-demand nanodevice with electrical and neuromorphic multifunction realized by local ion migration. *ACS Nano* **6**, 9515–9521 (2012).
9. Yin, J. et al. Adaptive crystallite kinetics in homogenous bilayer oxide memristor for emulating diverse synaptic plasticity. *Adv. Funct. Mater.* **28**, 1706927 (2018).
10. Zhou, F. et al. Optoelectronic resistive random access memory for neuromorphic vision sensors. *Nat. Nanotechnol.* **14**, 776–782 (2019).
11. Wu, C., Kim, T. W., Choi, H. Y., Strukov, D. B. & Yang, J. J. Flexible three-dimensional artificial synapse networks with correlated learning and trainable memory capability. *Nat. Commun.* **8**, 752 (2017).
12. Van de Burgt, Y. et al. A non-volatile organic electrochemical device as a low-voltage artificial synapse for neuromorphic computing. *Nat. Mater.* **16**, 414–418 (2017).
13. Ohno, T. et al. Short-term plasticity and long-term potentiation mimicked in single inorganic synapses. *Nat. Mater.* **10**, 591 (2011).
14. Zhao, X., Xu, H., Wang, Z., Lin, Y. & Liu, Y. Memristors with organic-inorganic halide perovskites. *InfoMat* **1**, 183–210 (2019).
15. Liu, C. et al. Small footprint transistor architecture for photoswitching logic and in situ memory. *Nat. Nanotechnol.* **14**, 662–667 (2019).
16. Li, B. et al. All-carbon electronic devices fabricated by directly grown single-walled carbon nanotubes on reduced graphene oxide electrodes. *Adv. Mater.* **22**, 3058–3061 (2010).
17. Cai, Y. et al. Extraordinarily stretchable all-carbon collaborative nanoarchitectures for epidermal sensors. *Adv. Mater.* **29**, 1606411 (2017).
18. Das, C., Kang, L. X., Ouyang, Q. L. & Yong, K. T. Advanced low-dimensional carbon materials for flexible devices. *InfoMat.* **2**, 698–714 (2020).
19. Amirsardari, Z., Aghdam, R. M., Salavati-Niasari, M. & Shakhesi, S. Enhanced thermal resistance of GO/C/phenolic nanocomposite by introducing ZrB2 nanoparticles. *Compos. Part B Eng.* **76**, 174–179 (2015).
20. Morteza Najarian, A., Szeto, B., Tefashe, U. M. & McCreery, R. L. Robust all-carbon molecular junctions on flexible or semi-transparent substrates using "Process-Friendly" fabrication. *ACS Nano* **10**, 8918–8928 (2016).
21. Shen, A. M. et al. Analog neuromorphic module based on carbon nanotube synapses. *ACS Nano* **7**, 6117–6122 (2013).

22. Kim, K., Chen, C. L., Truong, Q., Shen, A. M. & Chen, Y. A carbon nanotube synapse with dynamic logic and learning. *Adv. Mater.* **25**, 1693–1698 (2013).

23. Tian, H. et al. Graphene dynamic synapse with modulatable plasticity. *Nano Lett.* **15**, 8013–8019 (2015).

24. Sharbati, M. T. et al. Low-power, electrochemically tunable graphene synapses for neuromorphic computing. *Adv. Mater.* **30**, 1802353 (2018).

25. Sanchez Esqueda, I. et al. Aligned carbon nanotube synaptic transistors for large-scale neuromorphic computing. *ACS Nano* **12**, 7352–7361 (2018).

26. Jeong, H. Y. et al. Graphene oxide thin films for flexible nonvolatile memory applications. *Nano Lett.* **10**, 4381–4386 (2010).

27. Porro, S., Accornero, E., Pirri, C. F. & Ricciardi, C. Memristive devices based on graphene oxide. *Carbon* **85**, 383–396 (2015).

28. Kim, S. K. et al. Conductive graphitic channel in graphene oxide-based memristive devices. *Adv. Funct. Mater.* **26**, 7406–7414 (2016).

29. Liu, J. et al. Fabrication of flexible, all-reduced graphene oxide non-volatile memory devices. *Adv. Mater.* **25**, 233–238 (2013).

30. Raeber, T. J. et al. Resistive switching and transport characteristics of an all-carbon memristor. *Carbon* **136**, 280–285 (2018).

31. Garbin, D. et al. HfO2-based OxRAM devices as synapses for convolutional neural networks. *IEEE Trans. Electron. Dev.* **62**, 2494–2501 (2015).

32. Chen, Z. et al. Optimized learning scheme for grayscale image recognition in a RRAM based analog neuromorphic system. 2015 *International Electron Devices Meeting (IEDM)*, p. 17.7.1–17.7.4 (IEEE, Conference Location: Washington, DC, USA 2015).

33. Wu, W. et al. Improving analog switching in HfOx-based resistive memory with a thermal enhanced layer. *IEEE Electron Device Lett.* **38**, 1019–1022 (2017).

34. Du, C., Ma, W., Chang, T., Sheridan, P. & Lu, W. D. Biorealistic implementation of synaptic functions with oxide memristors through internal ionic dynamics. *Adv. Funct. Mater.* **25**, 4290–4299 (2015).

35. Pei, S. & Cheng, H. M. The reduction of graphene oxide. *Carbon* **50**, 3210–3228 (2012).

36. Stankovich, S. et al. Graphene-based composite materials. *Nature* **442**, 282 (2006).

37. Li, H. et al. Fluorescent N-doped carbon dots for both cellular imaging and highly-sensitive catechol detection. *Carbon* **91**, 66–75 (2015).

38. Ma, Z., Ming, H., Huang, H., Liu, Y. & Kang, Z. One-step ultrasonic synthesis of fluorescent N-doped carbon dots from glucose and their visible-light sensitive photocatalytic ability. *N. J. Chem.* **36**, 861–864 (2012).

39. Zhang, Z., Zheng, T., Li, X., Xu, J. & Zeng, H. Progress of carbon quantum dots in photocatalysis applications. *Part. Part. Syst. Char.* **33**, 457–472 (2016).

40. Yang, Y. et al. Fluorescent N-doped carbon dots as in vitro and in vivo nanothermometer. *ACS Appl. Mater. Int.* **7**, 27324–27330 (2015).

41. Liu, J. et al. Metal-free efficient photocatalyst for stable visible water splitting via a two-electron pathway. *Science* **347**, 970–974 (2015).

42. Zhang, W. et al. Enhanced photovoltaic effect of ruthenium complex-modified graphene oxide with P-type conductivity. *Mater. Chem. Phys.* **147**, 1140–1145 (2014).

43. Wang, H. et al. Photovoltaic properties of graphene oxide sheets beaded with ZnO nanoparticles. *J. Solid State Chem.* **184**, 881–887 (2011).

44. Jiang, B. et al. Enhanced photocatalytic activity and electron transfer mechanisms of graphene/TiO2 with exposed {001} facets. *J. Phys. Chem. C* **115**, 23718–23725 (2011).

45. Meng, N., Priestley, R. C. E., Zhang, Y., Wang, H. & Zhang, X. The effect of reduction degree of GO nanosheets on microstructure and performance of PVDF/GO hybrid membranes. *J. Membr. Sci.* **501**, 169–178 (2016).

46. Moon, I. K., Lee, J., Ruoff, R. S. & Lee, H. Reduced graphene oxide by chemical graphitization. *Nat. Commun.* **1**, 73 (2010).

47. Díez-Betriu, X. et al. Raman spectroscopy for the study of reduction mechanisms and optimization of conductivity in graphene oxide thin films. *J. Mater. Chem. C* **1**, 6905–6912 (2013).

48. Yang, J. J., Strukov, D. B. & Stewart, D. R. Memristive devices for computing. *Nat. Nanotechnol.* **8**, 13–24 (2013).

49. Zhao, X. et al. Photocatalytic reduction of graphene oxide–TiO2 nanocomposites for improving resistive-switching memory behaviors. *Small* **14**, 1801325 (2018).

50. Wang, Z., Ambrogio, S., Balatti, S. & Ielmini, D. A 2-transistor/1-resistor artificial synapse capable of communication and stochastic learning in neuromorphic systems. *Front. Neurosci.* **8**, 438 (2014).

51. Kim, S. et al. Experimental demonstration of a second-order memristor and its ability to biorealistically implement synaptic plasticity. *Nano Lett.* **15**, 2203–2211 (2015).

52. Yang, R. et al. Synaptic suppression triplet-STDP learning rule realized in second-order memristors. *Adv. Funct. Mater.* **28**, 1704455 (2018).

53. Zucker, R. S. & Regehr, W. G. Short-term synaptic plasticity. *Annu. Rev. Physiol.* **64**, 355–405 (2002).

54. Voglis, G. & Tavernarakis, N. The role of synaptic ion channels in synaptic plasticity. *EMBO Rep.* **7**, 1104–1110 (2006).

55. Atluri, P. P. & Regehr, W. G. Determinants of the time course of facilitation at the granule cell to Purkinje cell synapse. *J. Neurosci.* **16**, 5661–5671 (1996).

56. Kirkwood, A., Rioult, M. G. & Bear, M. F. Experience-dependent modification of synaptic plasticity in visual cortex. *Nature* **381**, 526 (1996).

57. Bear, M. F., Cooper, L. N. & Ebner, F. F. A physiological basis for a theory of synapse modification. *Science* **237**, 42–48 (1987).

58. Cooper, L. N. & Bear, M. F. The BCM theory of synapse modification at 30: interaction of theory with experiment. *Nat. Rev. Neurosci.* **13**, 798 (2012).

59. Suk, J. W. et al. Transfer of CVD-grown monolayer graphene onto arbitrary substrates. *ACS Nano* **5**, 6916–6924 (2011).

60. Li, X. et al. Transfer of large-area graphene films for high-performance transparent conductive electrodes. *Nano Lett.* **9**, 4359–4363 (2009).

61. Tang, Q. et al. Micrometer- and nanometer-sized organic single-crystalline transistors. *Adv. Mater.* **20**, 2947–2951 (2008).

62. Yablonovitch, E., Hwang, D., Gmitter, T., Florez, L. & Harbison, J. Van der Waals bonding of GaAs epitaxial liftoff films onto arbitrary substrates. *Appl. Phys. Lett.* **56**, 2419–2421 (1990).

63. Kumar, P. et al. Large-area reduced graphene oxide thin film with excellent thermal conductivity and electromagnetic interference shielding effectiveness. *Carbon* **94**, 494–500 (2015).

64. Tian, H. et al. A novel solid-state thermal rectifier based on reduced graphene oxide. *Sci. Rep.* **2**, 1–7 (2012).

65. Wang, M. et al. Robust memristors based on layered two-dimensional materials. *Nat. Electron.* **1**, 130–136 (2018).

66. Belhumeur, P. N., Hespanha, J. P. & Kriegman, D. J. Eigenfaces vs. fisherfaces: recognition using class specific linear projection. *IEEE Trans. Pattern Anal.* **19**, 711–720 (1997).

67. Gao, B. et al. Ultra-low-energy three-dimensional oxide-based electronic synapses for implementation of robust high-accuracy neuromorphic computation systems. *ACS Nano* **8**, 6998–7004 (2014).

68. Lin, Y. et al. Analog-digital hybrid memristive devices for image pattern recognition with tunable learning accuracy and speed. *Small Methods* **3**, 1900160 (2019).

69. Sheikh, H. R., Wang, Z., Bovik, A. & Simoncelli, E. Image quality assessment: from error visibility to structural similarity. *IEEE Trans. Image Process.* **13**, 600–612 (2004).